Chapter 4

THE STRUCTURE AND ENERGY OF GRAIN BOUNDARIES

4.1 INTRODUCTION

The majority of the book is concerned with the ways in which boundaries separating regions of different crystallographic orientation are formed or are rearranged on annealing either during or after deformation. In this chapter we will introduce some aspects of the structure and properties of these boundaries and in chapter 5 we discuss the migration and the mobility of boundaries. We will concentrate on those aspects of grain boundaries which are most relevant to recovery, recrystallization and grain growth and will not attempt to give a full coverage of the subject. Further information on grain boundaries may be found in the books by Hirth and Lothe (1968), Bollmann (1970), Gleiter and Chalmers (1972), Chadwick and Smith (1976), Balluffi (1980), Wolf and Yip (1992), Sutton and Balluffi (1995) and Gottstein and Shvindlerman (1999).

If we consider a grain boundary such as that shown in figure 4.1, the overall geometry of the boundary is defined by the orientation of the boundary plane AB with respect to one of the two crystals (two degrees of freedom) and by the smallest rotation (θ) required to make the two crystals coincident (three degrees of freedom). There are thus **five macroscopic degrees of freedom** which define the geometry of the boundary. In addition to this, the boundary structure is dependent on three **microscopic degrees of freedom,** which are the rigid body translations parallel and perpendicular to the boundary. The

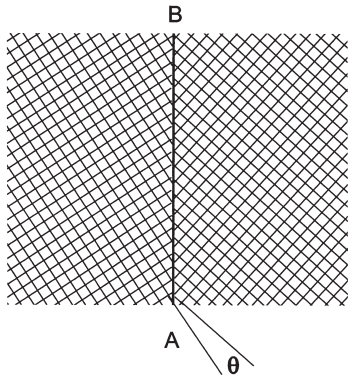

Fig. 4.1. A grain boundary between two crystals misoriented by an angle θ about an axis normal to the page.

structure of the boundary depends also on the local displacements at the atomic level and is influenced by external variables such as temperature and pressure, and internal parameters such as bonding, composition and defect structure. As many of the properties of a grain boundary are dependent on its structure, a knowledge of boundary structure is a necessary prerequisite to understanding its behaviour. Although there has been extensive experimental and theoretical work in this area over the past few decades, there is still a great deal of uncertainty about the structure and properties of boundaries. Most of this work has been carried out for **static boundaries** and there is even more uncertainty over the structure, energy and properties of the **migrating boundaries** which will be important during annealing. In addition, most of the experimental measurements have been made close to the melting temperature. We must therefore recognise that our ability to understand the phenomena of recovery, recrystallization and grain growth may well be limited by our lack of knowledge of the boundaries themselves.

It is convenient to divide grain boundaries into those whose misorientation is greater than a certain angle – **high angle grain boundaries (HAGB),** and those whose misorientation is less than this angle – **low angle grain boundaries (LAGB).** The angle at which the transition from low to high angle boundaries occurs is typically taken as **between 10° and 15°** and is to some extent dependent on what properties of the boundary are of interest. As a very general guide, low angle boundaries are those which can be considered to be composed of arrays of dislocations and whose structure and properties vary as a function of misorientation, whilst high angle boundaries are those whose structure and properties are not generally dependent on the misorientation. However, as discussed below, there are 'special' high angle boundaries which do have characteristic structures and properties, and therefore a crude division of boundaries into these two broad categories must be used with caution.

4.2 THE ORIENTATION RELATIONSHIP BETWEEN GRAINS

As discussed above, there are five macroscopic degrees of freedom needed to define a boundary. However, it is difficult to determine the orientation of the boundary plane

experimentally (§A2.6.3), and in many cases, we neglect it and consider only the three parameters which define the orientation between the two grains adjacent to a boundary. **It should however be recognised that the use of such an incomplete description of a boundary may cause problems in the interpretation of boundary behaviour.**

The relative orientation of two cubic crystals is formally described by the rotation of one crystal which brings it into the same orientation as the other crystal. This may be defined by the rotation matrix

$$R = \begin{bmatrix} a_{11} & a_{12} & a_{13} \\ a_{21} & a_{22} & a_{23} \\ a_{31} & a_{32} & a_{33} \end{bmatrix} \tag{4.1}$$

where a_{ij} are column vectors of direction cosines between the cartesian axes. The sums of the squares of each row and of each column are unity, the dot products between column vectors are zero, so only three independent parameters are involved. The rotation angle ($\boldsymbol{\theta}$) is given by

$$2\cos\theta + 1 = a_{11} + a_{22} + a_{33} \tag{4.2}$$

and the direction of the rotation axis **[uvw]** is given by

$$[(a_{32} - a_{23}), (a_{13} - a_{31}), (a_{21} - a_{12})]. \tag{4.3}$$

In cubic materials, because of the symmetry, the relative orientations of two grains can be described in **24** different ways. In the absence of any special symmetry, it is conventional to describe the rotation by the angle/axis pair associated with the **smallest** misorientation angle, and this is sometimes called the **disorientation.** The range of θ which can occur is therefore limited, and Mackenzie (1958) has shown that the maximum value of θ is 45° for $<100>$, 60° for $<111>$, 60.72° for $<110>$ and a maximum of 62.8° for $<1,1,\sqrt{2}-1>$. For a polycrystal containing grains of random orientation, the distribution of θ is as shown in figure 4.2, with a mean of 40°.

It should be emphasised that the misorientation distribution shown in figure 4.2 will only occur for a random grain assembly, and that a non-random distribution of orientations (i.e. a crystallographic texture) such as is normally found after thermomechanical processing, will alter the misorientation distribution. Examples of this are found in strongly textured material where the large volume of similarly oriented grains results in a large number of low/medium angle boundaries (e.g. figs. 14.3a, and A2.1), and in materials containing large numbers of special boundaries (i.e. the coincidence site boundaries discussed in §4.4.1) as shown in figure 11.8.

Figure 4.2 shows the distribution of misorientation angles regardless of the misorientation axes. However, if proximity to a specific misorientation axis is specified, the distribution may be markedly altered. For example figure 4.3 shows the distribution of misorientation angles predicted for a randomly oriented grain assembly in which only the axes closest to $<110>$ are considered. The curve now shows two peaks, and as demonstrated by Hutchinson et al. (1996), experimental observation of such peaks may

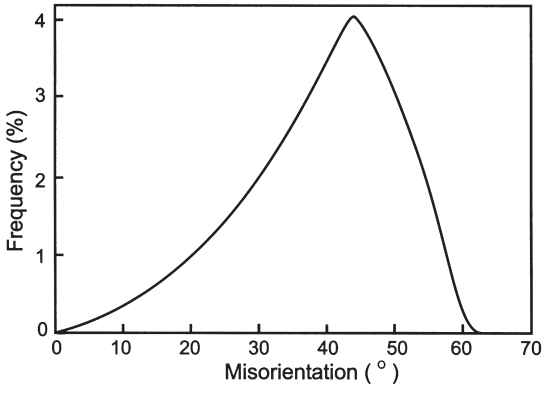

Fig. 4.2. The misorientation distribution for a randomly oriented assembly of grains.

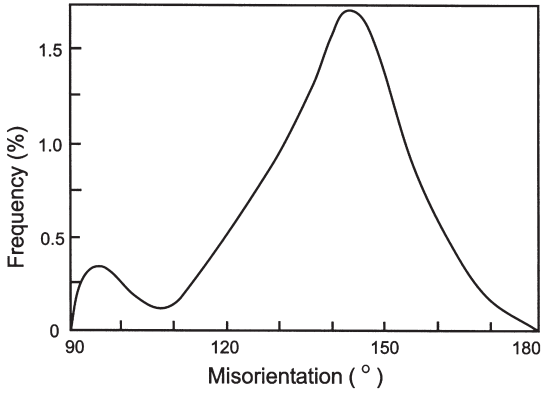

Fig. 4.3. The distribution of misorientation angles for a randomly oriented assembly of grains, for rotation axes closest to $<110>$, (after Hutchinson et al. 1996).

be wrongly interpreted as evidence of a predominance of boundaries with special orientation relationships.

As discussed in appendix 2, the technique of electron backscatter diffraction (EBSD), allows misorientation distributions of the type shown in figure 4.2, sometimes known as **Mackenzie plots,** to be readily obtained. As shown in figure A2.1, such plots provide an excellent 'fingerprint' of the microstructure, and are likely to become extensively used in the future.

The **angle/axis** notation described above is commonly used to express misorientations. However, there are several other ways of expressing the orientation relationship, including Euler angles (**misorientation distribution functions**) and **Rodrigues-Frank space.** The use of these methods for describing absolute orientations is outlined in appendix 1 and will not be further considered here.

4.3 LOW ANGLE GRAIN BOUNDARIES

A low angle boundary or sub-boundary can be represented by an array of dislocations (Burgers 1940, Read and Shockley 1950). The simplest such boundary is the symmetrical **tilt boundary,** shown schematically in figure 4.4 in which the lattices on either side of the boundary are related by a misorientation about an axis which lies in the plane of the boundary. The boundary consists of a wall of parallel edge dislocation aligned perpendicular to the slip plane. Such boundaries were first revealed as arrays of etch pits on the surface of crystals, but are now more commonly observed by transmission electron microscopy.

4.3.1 Tilt boundaries

If the spacing of the dislocations of Burgers vector **b** in the boundary is **h**, then the crystals on either side of the boundary are misoriented by a small angle θ, where

$$\theta \approx \frac{b}{h}. \tag{4.4}$$

The energy of such a boundary γ_s, is given (Read and Shockley 1950) as:

$$\gamma_s = \gamma_0 \theta(A - \ln \theta) \tag{4.5}$$

where $\gamma_0 = Gb/4\pi(1 - v)$, $A = 1 + \ln(b/2\pi r_0)$ and r_0 is the radius of the dislocation core, usually taken as between b and 5b.

According to this equation, the energy of a tilt boundary increases with increasing misorientation (decreasing **h**) as shown in figure 4.5. Combining equations 4.4 and 4.5 we note that as θ increases, the energy **per dislocation** decreases as shown in figure 4.5, showing that a material will achieve a lower energy if the same number of dislocations are arranged in fewer, but higher angle boundaries. As shown in figure 4.6, the theory is in good agreement with experimental measurements for small values of θ, although it is

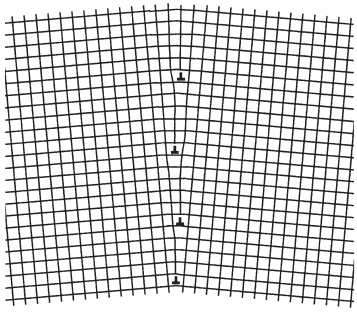

Fig. 4.4. A symmetrical tilt boundary.

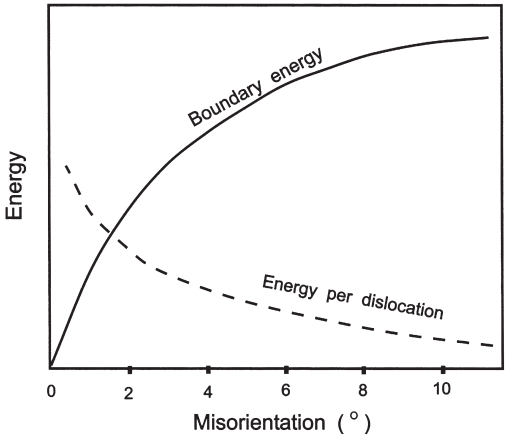

Fig. 4.5. The energy of a tilt boundary and the energy per dislocation as a function of the crystal misorientation.

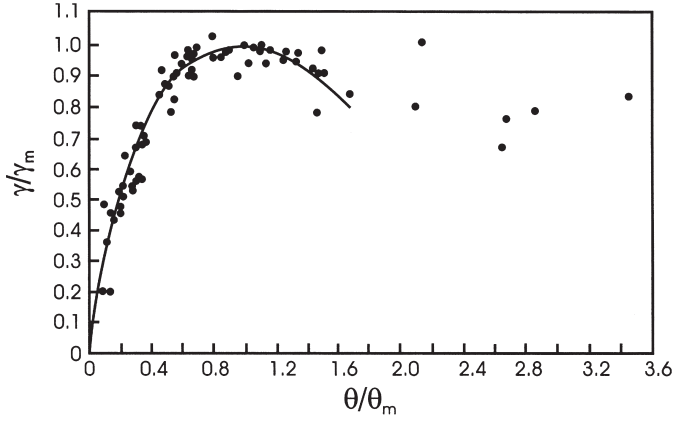

Fig. 4.6. The measured (symbols) and calculated (solid line) energy of low angle tilt boundaries as a function of misorientation, for various metals, (after Read 1953).

unreasonable to use this dislocation model for large misorientations, because when θ exceeds $\sim 15^\circ$, the dislocation cores will overlap, the dislocations lose their identity and the simple dislocation theory on which equation 4.5 is based becomes inappropriate.

It is often convenient (Read 1953) to use equation 4.5 in a form where the boundary energy (γ_s) and misorientation (θ) are normalised with respect to the values of these parameters (γ_m and θ_m) when the boundary becomes a high angle boundary (i.e. $\theta \sim 15^\circ$).

$$\gamma = \gamma_m \frac{\theta}{\theta_m}\left(1 - \ln\frac{\theta}{\theta_m}\right) \tag{4.6}$$

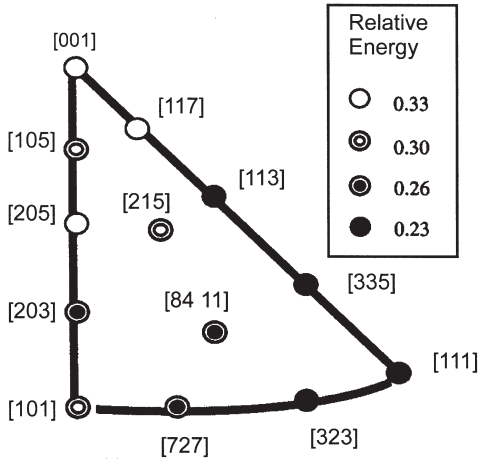

Fig. 4.7. The variation of the energy of low angle grain boundaries with misorientation axis, (after Yang et al. 2001).

Although the Read-Shockley relationship is widely used, there have been very few experimental measurements of the energy of low angle boundaries. However, detailed measurements of triple junction geometry and crystallography in polycrystalline aluminium foils, accompanied by statistical analysis have recently been used to determine boundary energies by Yang et al. (2001). The results show good agreement with the Read–Shockley relationship (equation 4.6). These authors also found a small dependence of the energy of low angle boundaries on the misorientation axis as shown in figure 4.7, with axes close to $<100>$ having the highest energy and those close to $<111>$ the lowest.

4.3.2 Other low angle boundaries

In the more general case, dislocations of two or more Burgers vectors react to form two-dimensional networks whose character depends on the types of dislocation involved. For example a **twist** boundary, which is a boundary separating crystals related by a misorientation about an axis lying perpendicular to the boundary plane, may be formed by two sets of screw dislocations. If the Burgers vectors of the two sets of dislocations are orthogonal then the dislocations do not react strongly and the boundary consists of a square network of dislocations (fig. 4.8a,c). However, if the Burgers vectors are such that the two sets of dislocations react to form dislocations of a third Burgers vector as shown in figure 4.8b,d then a hexagonal network may be formed. If **h** is the spacing of the dislocations in the network the misorientation (θ) is given approximately by equation 4.4. The exact shape of the dislocation network will depend on the angle that the boundary plane makes with the crystals. Further details of the reactions involved in forming low angle grain boundaries may be found in textbooks on dislocation theory (e.g. Friedel 1964, Hirth and Lothe 1982, Hull and Bacon 2001).

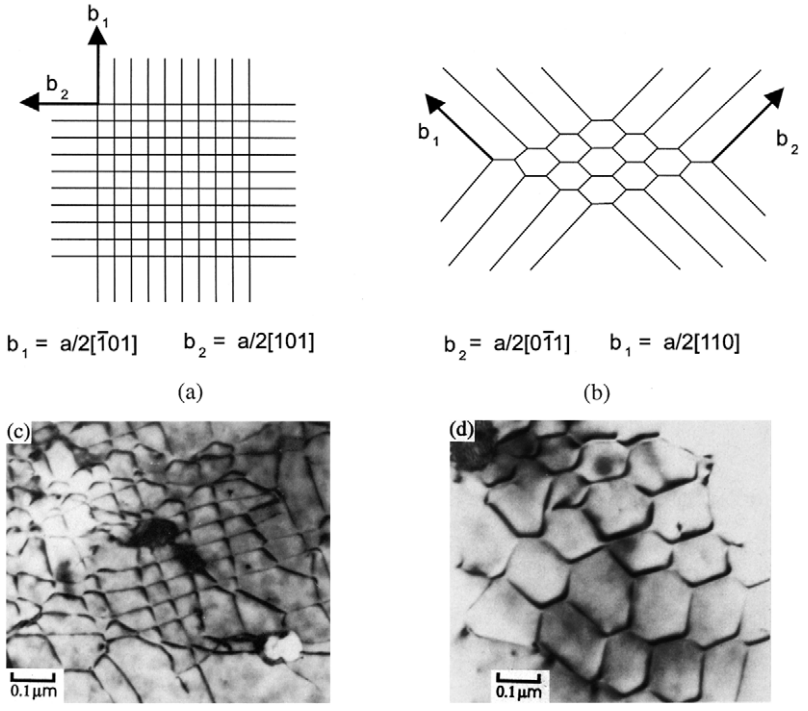

Fig. 4.8. The formation of low angle twist boundaries from dislocation arrays. (a) A square network formed from screw dislocations of orthogonal Burgers vector, (b) A hexagonal network formed by screw dislocations with 120° Burgers vectors, (c) TEM micrograph of a square twist boundary in copper, (Humphreys and Martin 1968), (d) TEM micrograph of a hexagonal twist boundary in copper, (Humphreys and Martin 1968).

4.4 HIGH ANGLE GRAIN BOUNDARIES

Although the structure of low angle grain boundaries is reasonably well understood, much less is known about the structure of high angle grain boundaries. Early theories suggested that the grain boundary consisted of a thin 'amorphous layer' (§1.2.1), but it is now known that these boundaries consist of regions of good and bad matching between the two grains. The concept of the **coincidence site lattice (CSL)** (Kronberg and Wilson 1949), and extensive computer modelling, together with atomic resolution microscopy have in recent years considerably advanced the subject.

4.4.1 The coincidence site lattice

Consider two interpenetrating crystal lattices and translate them so as to bring a lattice point of each into coincidence, as in figure 4.9. If other points in the two lattices coincide

Table 4.1
Rotation axes and angles for coincidence site lattices of Σ < 31.

Σ	θ°_{min}	Axis	Frequency %
1	0	Any	2.28
3	60	< 111 >	1.76
5	36.87	< 100 >	1.23
7	38.21	< 111 >	0.99
9	38.94	< 110 >	1.02
11	50.48	< 110 >	0.75
13a	22.62	< 100 >	0.29
13b	27.80	< 111 >	0.39
15	48.19	< 210 >	0.94
17a	28.07	< 100 >	0.20
17b	61.93	< 221 >	0.39
19a	26.53	< 110 >	0.33
19b	46.83	< 111 >	0.22
21a	21.79	< 111 >	0.19
21b	44.40	< 211 >	0.57
23	40.45	< 311 >	0.50
25a	16.25	< 100 >	0.11
25b	51.68	< 331 >	0.44
27a	31.58	< 110 >	0.20
27b	35.42	< 210 >	0.39
29a	43.61	< 100 >	0.09
29b	46.39	< 221 >	0.35

Data from Mykura 1980. Column 4, lists the frequencies of the occurrence of the boundaries predicted for a random grain assemble (Pan and Adams 1994), using the Brandon criterion.

(the solid circles in fig. 4.9), then these points form the coincident site lattice. The reciprocal of the ratio of CSL sites to lattice sites is denoted by **Σ.** For example in figure 4.9, Σ is seen to be 5. In the general case where there is no simple orientation relationship between the grains, Σ is large and the boundary, which has no special properties, is often referred to as a **random boundary.** However, for certain orientation relationships for which there is a good fit between the grains, Σ is small and this may confer some special properties on the boundary. Good examples of this are the coherent twin (Σ3) boundary shown in figure 4.10, low angle grain boundaries (Σ1), and the high mobility Σ7 boundaries in fcc materials which are discussed in §5.3.2.

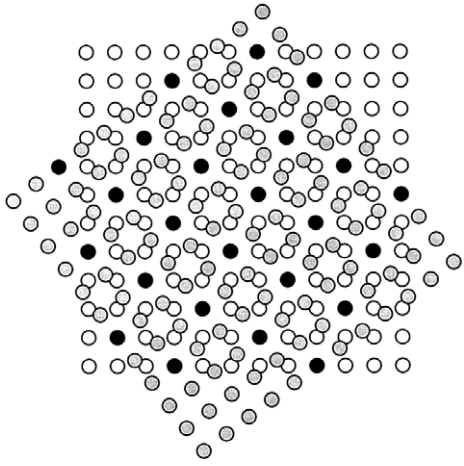

Fig. 4.9. A coincident site lattice (Σ5) formed from two simple cubic lattices rotated by 36.9° about an $<001>$ axis. Filled circles denote sites common to both lattices.

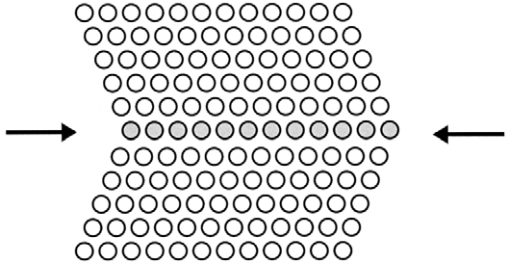

Fig. 4.10. A coherent twin (Σ3) boundary.

The concept of **Grain Boundary Engineering,** in which the properties of the material are improved by processing the material so as to maximise the number of CSL or 'special' boundaries has been developed in recent years (Watanabe 1984), and is discussed in more detail in §11.3.2.3.

Further details of the geometry of CSL boundaries and extensive tables of CSL relationships may be found in Brandon et al. (1964), Grimmer et al. (1974), Mykura (1980) and Warrington (1980). Table 4.1 shows the relationship between Σ and the angle/axis rotation for boundaries up to and including Σ29.

4.4.2 The structure of high angle boundaries

The atomic structure at the grain boundary is determined by relaxation of the atoms, which is dependent on the nature of the atomic bonding forces, and there has been

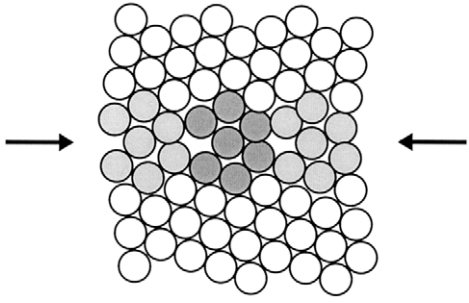

Fig. 4.11. The repeating structural units in a special grain boundary, (after Gleiter 1971).

extensive computer simulation of these structures (e.g. Gleiter 1971, Weins 1972, Vitek et al. 1980, Balluffi 1982, Wolf and Merkle 1992). It is predicted that a high degree of atomic-level coherency is maintained across the boundary and that regular, well defined **structural units** are formed. In the boundary of figure 4.11, the repeating structural units are shaded.

The CSL is a geometric relationship and any deviation from the exact coincidence relationship discussed above will destroy the CSL. However, even in this situation the boundary structure can be maintained by introducing **grain boundary dislocations** which can locally accommodate the mismatch in much the same way as dislocations preserve the lattice in low angle ($\Sigma 1$) grain boundaries. The Burgers vector of the boundary dislocations can be much smaller than a lattice vector. It is also predicted (King and Smith 1980) that some grain boundary dislocations are associated with **steps** in the boundary. These boundary defects are of importance in the mobility of boundaries and are discussed further in §5.4.1.3.

The structure of grain boundaries has been extensively investigated by high resolution electron microscopy and other techniques (e.g. Gronski 1980, Pond 1980, Sass and Bristowe 1980, Krakow and Smith 1987, Seidman 1992, Wolf and Merkle 1992). The experimental observations have broadly confirmed the computer calculations and show that although the CSL is generally lost during the atomic relaxation at the boundaries, the periodicity of the boundary structure is retained by a network of grain boundary dislocations.

A CSL boundary which deviates from the exact relationship by an angle $\Delta\theta$ but in which the structure is maintained by an array of grain boundary dislocations may still possess the special properties appropriate to the CSL boundary, and it is therefore useful to define $\Delta\theta$. As $\Delta\theta$ increases, the spacing of the boundary dislocations decreases (equation 4.4) and the limiting value of $\Delta\theta$ will be reached when the dislocation cores overlap. The angular deviation limit will be related to the periodicity of the boundary, and is often taken as the **Brandon criterion** (Brandon 1966).

$$\Delta\theta \leq 15\Sigma^{-1/2} \tag{4.7}$$

Observations of discrete grain boundary dislocations and measurements of the properties of special boundaries (see e.g. Palumbo and Aust 1992, Randle 1996) suggest that this criterion is too lax and that a better limit is

$$\Delta\theta \leq 15\Sigma^{-5/6}. \tag{4.8}$$

4.4.3 The energy of high angle boundaries

On the basis of the structural models outlined above, it might be expected that the energy of the boundary would be a minimum for an exact coincidence relationship and that it would increase as the orientation deviated from this, due to the energy of the network of accommodating boundary dislocations. However, the correlation between the **geometry** and the **energy** of a boundary is more complicated than this

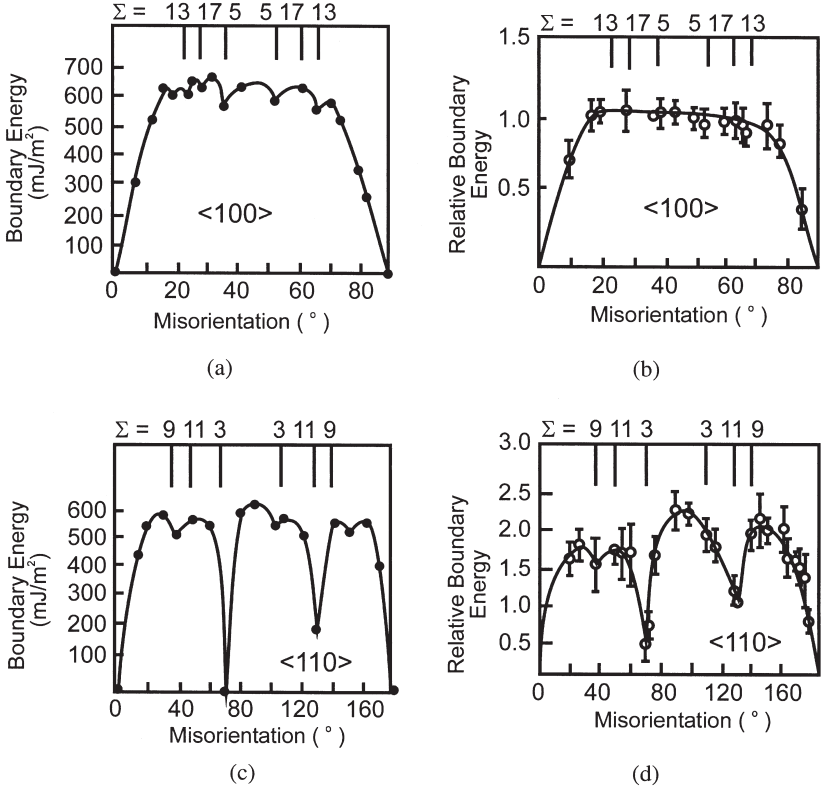

Fig. 4.12. The computed (a) and (c) and measured (b) and (d) energies at 650°C for symmetrical <100> and <110> tilt boundaries in aluminium, (Hasson and Goux 1971).

(Goodhew 1980) as is illustrated by figure 4.12 which shows a comparison of the measured and calculated energies of symmetrical tilt boundaries in aluminium. It can be seen that low energy cusps are found only for the $\Sigma 3$ (coherent twin) and $\Sigma 11$ boundaries and that the predicted cusps for $\Sigma 5$ and $\Sigma 9$ are not detected. However, more recent measurements of boundary energies in high purity metals (e.g. Miura et al. 1990, Palumbo and Aust 1990) have found evidence for more low energy special boundaries than were found in earlier work.

The experimental measurements of boundary energy have been reviewed by Palumbo and Aust (1992). It is suggested that the lack of low energy cusps may in some cases be due to an insensitivity in the measurement technique and in other cases be due to small amounts of impurity. There is evidence that the energy and presumably the structure of high angle boundaries is affected by impurity segregation. Measurements of boundary energy in Ag–Au and Cu–Pb (Gleiter 1970a, Sauter et al. 1977) suggest that with increasing segregation, the energy of special grain boundaries tends towards that of random boundaries as shown schematically in figure 4.13, and more recent experiments (Palumbo and Aust 1992) have confirmed this trend.

Sutton and Balluffi (1987) concluded from a survey of the experimental measurements that there is no simple relationship between the energy of a boundary and the overall **geometry** of the boundary as defined by the macroscopic degrees of freedom, and that parameters such as a low value of Σ were not necessarily indicative of a low energy. It is likely that the boundary energy is determined primarily by the **microscopic** structure of the boundary and that atomic bonding plays an important role. Computer simulations (Smith et al. 1980, Wolf and Merkle 1992) suggest that the local **volume expansion** or **free volume** associated with a boundary is important, and the latter authors predict a linear relationship between boundary energy and volume expansion.

Some caution is however needed in interpreting the experimental measurements of boundary energy and applying these to the annealing processes considered later in this

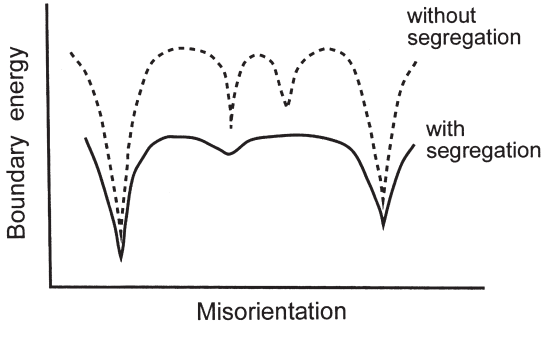

Fig. 4.13. Schematic diagram showing the changes in the energy versus misorientation relationship due to solute atoms, with and without segregation at the boundaries, (Sauter et al. 1977).

Table 4.2
Measured grain boundary energies (mJm^{-2}) (Data from Murr 1975).

Material	High angle grain boundary energy	Coherent twin boundary energy	Incoherent twin boundary energy
Ag	375	8	126
Al	324	75	—
Au	378	15	—
Cu	625	24	498
Cu–30 wt% Zn	595	14	—
Fe (γ)	756	—	—
Fe–3 wt% Si	617	—	—
Stainless steel (304)	835	19	209
Ni	866	43	—
Sn	164	—	—
Zn	340	—	—

book, because such measurements are normally made at very high homologous temperatures in order for equilibrium to be achieved. There is evidence both from experiments (Gleiter and Chalmers 1972, Goodhew 1980, Shvindlerman and Straumal 1985, Rabkin et al. 1991, Sutton and Balluffi 1995, Gottstein and Shvindlerman 1999), and molecular dynamic simulations (Wolf 2001) that some special boundaries may exhibit a **phase transition** at very high temperatures, and that this may involve either a transformation to a different ordered structure or to a liquid-like structure. Such transitions will have significant effects on the boundary energies and on other properties such as diffusion and mobility, as is further discussed in §5.3.1.

It is to be expected that the structure and hence the energy of a special boundary will be dependent on the actual plane of the boundary, as demonstrated by Lojkowski et al. (1988). As shown in table 4.2, the energy of the $\Sigma 3$ coherent twin boundary is much smaller than that of the non-coherent boundary.

4.5 THE TOPOLOGY OF BOUNDARIES AND GRAINS

In addition to the structure and properties of individual grain boundaries we need to be aware of the arrangements of boundaries within a material. As boundaries are non-equilibrium defects, a single-phase material is in its most thermodynamically stable state when all boundaries are removed. This is not often achieved and much of this book is devoted to a discussion of the processes by which high and low angle boundaries are eliminated or rearranged into metastable configurations. In this section we consider the nature of these metastable arrangements of boundaries.

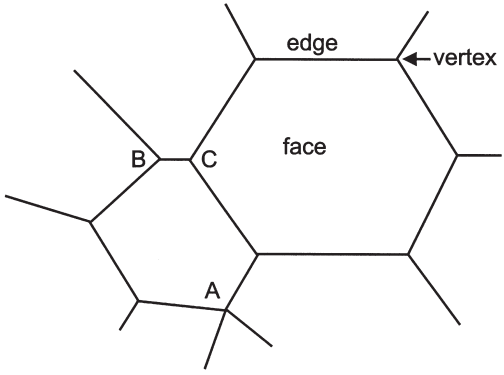

Fig. 4.14. A 2-D section of a grain structure. The 4-rayed vertex at **A** will tend to decompose into two 3-rayed vertices such as **B** and **C**.

C.S. Smith set out the topological requirements of space-filling and the role of boundary tensions in his classic paper of 1952 and these have been reviewed by Atkinson (1988). In both 2-D and 3-D, the microstructure consists of **vertices** joined by **edges** or **sides** which surround **faces** as shown schematically in figure 4.14. In the 3-D case, the faces surround **cells** or **grains.** The cells, faces, edges and vertices of any cellular structure obey the conservation law of equation 4.9, known as **Euler's equation,** provided that the face or cell at infinity is not counted.

$$\begin{aligned} F - E + V &= 1 \text{ (2-D plane)} \\ -C + F - E + V &= 1 \text{ (3-D Euclidean space)} \end{aligned} \tag{4.9}$$

where **C** is the number of cells, **E** edges, **F** faces and **V** vertices.

The number of edges joined to a given vertex is its coordination number **z.** For topologically stable structures, $z = 3$ in 2-D and $z = 4$ in 3-D. Thus in 2-D, a 4-rayed vertex such as that shown at A in figure 4.14 will be unstable and will decompose to two 3-rayed vertices such as B and C.

4.5.1 Two-dimensional microstructures

In a two-dimensional microstructure, the material will be divided into grains or subgrains separated by boundaries and, if boundaries are mobile, a local mechanical equilibrium will be established at the vertices of grains. Consider the three grains 1, 2 and 3 shown in figure 4.15. The boundaries have specific energies γ_{12}, γ_{13}, and γ_{23}, and at equilibrium these energies are equivalent to boundary tensions per unit length. For the three boundaries of figure 4.15 the stable condition is

$$\frac{\gamma_{12}}{\sin\alpha_3} = \frac{\gamma_{13}}{\sin\alpha_2} = \frac{\gamma_{23}}{\sin\alpha_1} \tag{4.10}$$

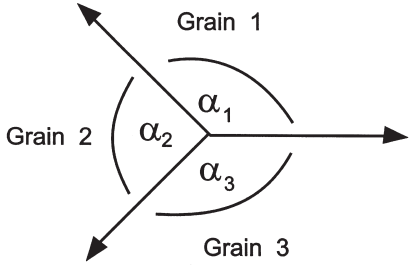

Fig. 4.15. The forces at a boundary triple point.

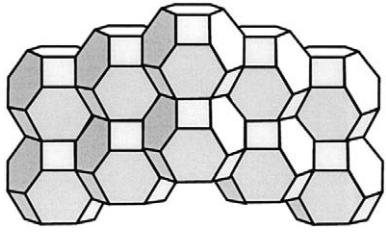

Fig. 4.16. Body centred cubic packing of truncated octahedra, (after Smith 1952).

If all boundaries have the same energy, then equation 4.10 shows that the three grains will meet at angles of 120°. In this situation an array of equal sized hexagonal grains would be stable. Whatever the actual arrangement of the grains in a two-dimensional microstructure, it follows from equation 4.9 that if $z = 3$, the mean number of sides per grain or cell is 6.

4.5.2 Three-dimensional microstructures

It has been shown (Smith 1952) that there is no three-dimensional plane-faced polyhedron which, when repeated, can simultaneously completely fill space and balance the boundary tensions. Truncated octahedra stacked in a bcc arrangement as shown in figure 4.16 come close, filling the space but not having the correct angles to balance the boundary forces. The **Kelvin tetrakaidecahedron,** figure 4.17, which has doubly curved boundary surfaces satisfies both conditions.

Polycrystalline materials are usually examined on a random planar section and therefore sectioning effects will mean that the angles measured on the microstructure will not necessarily be the true boundary angles. However, in microstructures of well annealed single-phase materials, the sectioned grains often approximate to hexagons, and it has been shown (Smith 1948) that the distribution of measured angles is Gaussian, peaking at the true angle. Figure 4.18 shows some measurements for high angle grain

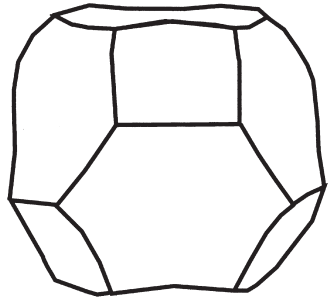

Fig. 4.17. The Kelvin tetrakaidecahedron.

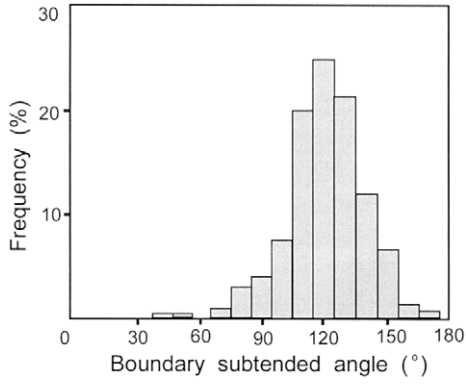

Fig. 4.18. The frequency of grain boundary angles for high energy boundaries in α-brass, (after Smith 1948).

boundaries in annealed α-brass. It may be seen that the data peak at 120° which is the equilibrium angle.

If, as is usually the case, the boundary energies are not equal, the regular geometric structures discussed above will not be stable. An example of this is the microstructure of recrystallized α-brass, shown in figure 7.36, which contains both normal or 'random' high angle boundaries and low energy $\Sigma 3$ coherent twins. The lower energy of the twin boundaries is apparent from the angles, little larger than 90° which they make with the random high angle boundaries at **A.** This should be compared with the angles at the triple point **B** involving only high energy boundaries. For similar reasons, low angle grain boundaries whose energies are strongly dependent on misorientation (fig. 4.6) are rarely arranged at 120° to each other as seen in the recovered microstructure shown in figure 6.21.

The instability resulting from the interaction between the space-filling requirements and the boundary tensions, provides the driving pressure for the growth of subgrains and grains which are discussed in later chapters.

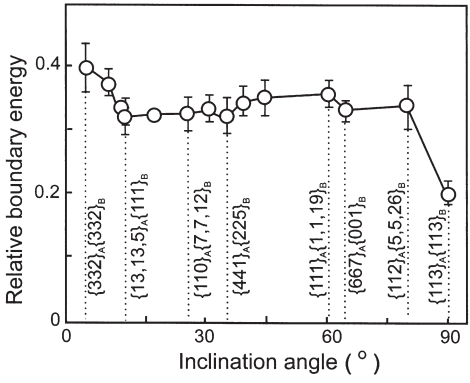

Fig. 4.19. The relative boundary energy for asymmetric [110] Σ11 tilt boundaries in copper, as a function of boundary inclination, (after Goukon et al. 2000).

4.5.3 Grain boundary facets

The example of Σ3 twin boundaries discussed above and shown in figure 7.36, is an extreme example of grain boundaries developing facets. Faceting of grain boundaries has long been known to occur in many metals (see e.g. Sutton and Balluffi 1995, Gottstein and Shvindlerman 1999). In order for a boundary to be facetted spontaneously, the decrease in the total boundary energy must overcome the increase in the total boundary area. Faceting is therefore only likely to occur under conditions when the boundary energy depends strongly on the boundary plane, and the most common situation is for low energy CSL boundaries. It is found that the faceting behaviour of a particular boundary may be strongly dependent on the impurity level (Ference and Balluffi 1988), and on the temperature (Hsieh and Balluffi 1989). Figure 4.19 shows the effect of boundary inclination angle on the relative energies of asymmetric Σ11 {110] boundaries in copper (Goukon et al. 2000) and this has been found to correlate well with the faceting behaviour. Faceting of the boundaries of recrystallizing grains is also sometimes observed (§5.3.2.2), and an example is seen in figure 5.16.

4.5.4 Boundary connectivity

The importance of non-random distribution of grain **orientations** or texture is widely recognised and discussed in detail in chapters 3 and 12. However, it has also been suggested that the non-random spatial distribution of grain **misorientations** may also be important, particularly for CSL boundaries. If such boundaries have values of properties such as strength or diffusivity which are markedly different from the other boundaries, then clustering effects and their linking or **connectivity** may have an influence on the chemical, physical or mechanical properties of the material (Watanabe 1994), and such effects are an important consideration in **grain boundary engineering** (§11.3.2.3).

4.5.5 Triple junctions

Although in this chapter we are mainly concerned with the properties of the grain faces or boundaries, there is evidence that the properties of the vertices or **triple junctions** may play a role in microstructural evolution and have an influence on grain growth and this is considered in §5.5.

4.6 THE INTERACTION OF SECOND-PHASE PARTICLES WITH BOUNDARIES

A dispersion of particles will exert a retarding force or pressure on a low angle or high angle grain boundary and this may have a profound effect on the processes of recovery, recrystallization and grain growth. The effect is known as **Zener drag** after the original analysis by Zener which was published by Smith (1948). The magnitude of this interaction depends the nature of the particle and interface, and the shape, size, spacing and volume fraction of the particles. The definitions of the parameters of a second phase distribution are given in appendix 2.8.

4.6.1 The drag force exerted by a single particle

4.6.1.1 General considerations

Let us consider first, the interaction of a boundary of specific energy γ with a spherical particle of radius **r** which has an incoherent interface.

If the boundary meets the particle at an angle β as shown in figure 4.20 then the restraining force on the boundary is:

$$F = 2\pi r\gamma \cos\beta \sin\beta \tag{4.11}$$

The maximum restraining effect (F_S) is obtained when $\beta = 45^\circ$, when

$$F_S = \pi r\gamma \tag{4.12}$$

As discussed by Nes et al. (1985), there have been many different derivations of this force, but the result is usually similar to the above. It should be noted that when a boundary intersects a particle, the particle effectively removes a region of boundary

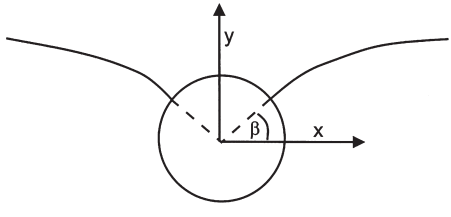

Fig. 4.20. The interaction between a grain boundary and a spherical particle.

equal to the intersection area and thus the energy of the system is lowered, and boundaries are therefore **attracted** to particles.

Equation 4.12 predicts that the pinning force exerted by a particle should be proportional to the grain boundary energy (γ). Therefore we expect the pinning due to low angle boundaries and low energy Σ boundaries to be less than for 'random' high angle boundaries. There is surprisingly little evidence of this, although Humphreys and Ardakani (1996) showed that in copper, the pinning pressure on boundaries close to $40^\circ < 111 >$ ($\Sigma 7$) was some 10% smaller than for other high angle boundaries.

4.6.1.2 The effect of particle shape

The particle shape, if not spherical, will have some effect on the pinning force (Ryum et al. 1983, Nes et al. 1985). The latter authors considered the interaction of a boundary with an ellipsoidal particle as shown in figure 4.21. Their treatment assumes that the grain boundary meets the particle at an angle of 90° and that the particle makes a planar hole in the boundary. They calculated the drag force for the two extreme cases shown in figure 4.21, and showed that the maximum forces were

Case 1
$$F_1 = F_S\left(\frac{2}{(1+e)\,e^{1/3}}\right) \tag{4.13}$$

Case 2 for $e \geq 1$
$$F_2 = F_S\left(\frac{1+2.14e}{\pi\, e^{1/2}}\right) \tag{4.14}$$

Case 2 for $e \leq 1$
$$F_2 = F_S\, e^{0.47} \tag{4.15}$$

where **e** is the eccentricity of the ellipsoidal particle. When $\mathbf{e} = 1$ then the particle is a sphere, and F_S is the drag from a spherical particle of the same volume. Figure 4.22 shows how F_1 and F_2 vary with aspect ratio for a particle of constant volume. It can be seen that the pinning force is only significantly larger than that of a spherical particle

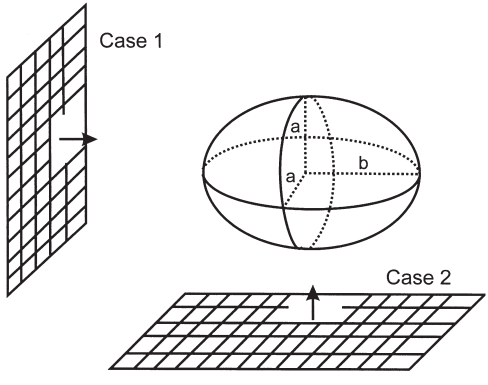

Fig. 4.21. The interaction of boundaries with an ellipsoidal particle, (after Nes et al. 1985).

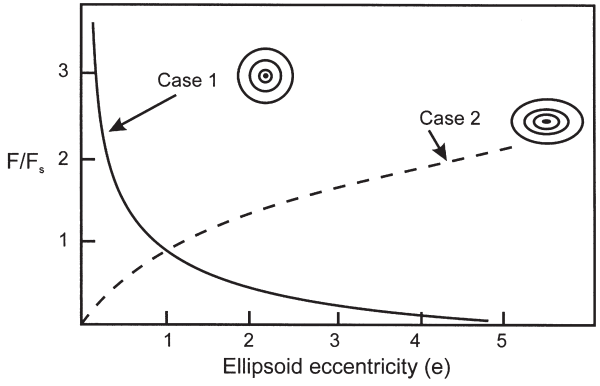

Fig. 4.22. The drag force as a function of particle aspect ratio for the two cases illustrated in figure 4.21, (after Nes et al. 1985).

for the case of thin plates meeting the boundary face-on and long needles meeting the boundary edge-on.

Ringer et al. (1989) have analysed the interaction of a boundary with cubic particles. The strength of the interaction depends upon the orientation of the cube relative to the boundary and in the extreme case, when the cube side is parallel to the boundary, the drag force is almost twice that of a sphere of the same volume. However, as this is a special case, it is unlikely to be a very significant factor in practice.

4.6.1.3 Coherent particles

If a high angle grain boundary moves past a coherent particle then the particle will generally lose coherence during the passage of the boundary. As the energy of the incoherent interface is greater than that of the original coherent interface, energy is required to cause this transformation, and this energy must be supplied by the moving boundary. Therefore, as first shown by Ashby et al. (1969), coherent particles will be more effective in pinning boundaries than will incoherent particles.

Following the analysis by Nes et al. (1985), if the grains are denoted 1 and 2 and the particle as 3, as in figure 4.23a, then there are now three different boundary energies γ_{12}, γ_{13} and γ_{23}. These boundaries meet at the particle surface, and if equilibrium is established then

$$\gamma_{23} = \gamma_{31} + \gamma_{12}\cos\alpha \tag{4.16}$$

and

$$\cos\alpha = \frac{\gamma_{23} - \gamma_{13}}{\gamma_{12}} \tag{4.17}$$

The drag force is then

$$F_C = 2\pi r\gamma\cos(\alpha - \theta)\cos\theta \tag{4.18}$$

F_C is a maximum when $\theta = \alpha/2$ and $\alpha = 0$, giving

$$F_C = 2\pi r\gamma \tag{4.19}$$

Thus coherent particles are twice as effective in pinning a grain boundary as incoherent particles of the same size.

The passage of a high angle boundary past a coherent particle, results in the particle losing coherency. As a small incoherent particle will be less stable (Gibbs-Thomson effect), there are a number of alternative interactions. For example the particle may **dissolve** during passage of the boundary and **re-precipitate** in a coherent orientation, it may **reorient** itself to a coherent orientation, or the boundary may **cut** through the particle (Doherty 1982).

Dissolution – There is experimental evidence that small coherent particles can be dissolved by a moving boundary. The problem has been discussed by Doherty (1982) and by Nes et al. (1985). The latter authors show that in these circumstances the pinning force due to a coherent particle is dependent not only on the particle size, but also on the concentration of the alloy. The pinning force is given by

$$F = \frac{2\pi AkTr^2}{3V}\ln\left(\frac{C_0}{C_{eq}}\right) - 2\pi\gamma' r \tag{4.20}$$

where A = Avogadro's number, k = Boltzmann's constant, V is the molar volume of the precipitate phase, C_0 is solute concentration, C_{eq} is the equilibrium concentration and γ' is the energy of the coherent interface.

Following dissolution, the particles may re-precipitate coherently behind the grain boundary or alternatively discontinuous precipitation may occur at the boundary.

Coherent particles on a stationary boundary – If there is insufficient driving force for a boundary to move past the coherent particles or to dissolve them then the particles will become incoherent along the boundary. As a consequence of this, the equilibrium shape of the particles on the boundary will alter as shown in figure 4.23b. The increase in radius of curvature of the particles on the boundary will then cause them to coarsen at the expense of the smaller spherical coherent particles, thus increasing the pinning of the boundary (Howell and Bee 1980).

Passage of boundary through coherent particles – In some circumstances the precipitate may be cut by the boundary and undergo the same orientation change as the grain surrounding it, as shown in figure 4.23c. This has been observed in nickel alloys containing the coherent γ' phase (Porter and Ralph 1981, Randle and Ralph 1986), and in aluminium alloys containing semi-coherent Al_3Sc particles (Jones and Humphreys 2001).

4.6.2 The drag pressure due to a distribution of particles

Having considered the pinning force from a single particle, we now need to calculate the restraining pressure on the boundary due to an array of particles. This is a complicated problem which has not yet been completely solved.

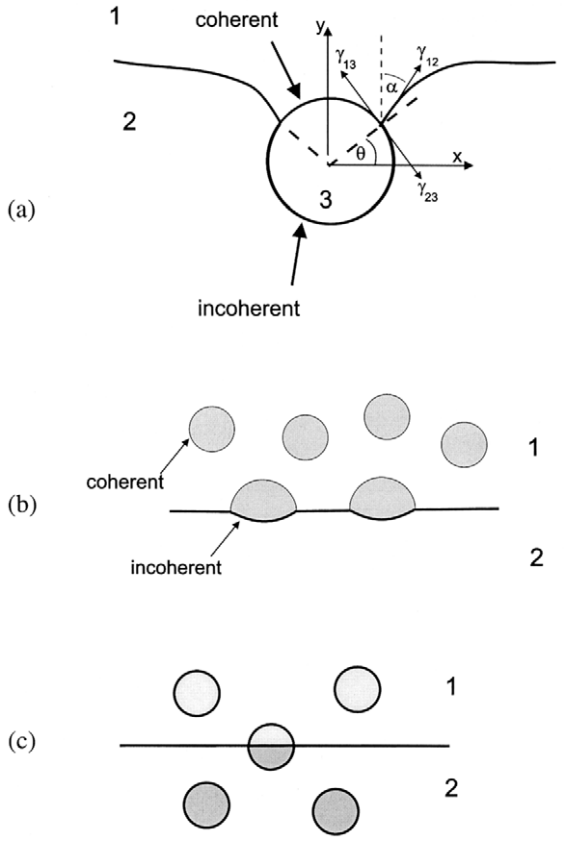

Fig. 4.23. The interaction between a coherent particle and a high angle grain boundary. (a) The boundary by-passes the particle; (b) The boundary halts at the particles; (c) The boundary cuts through the particle.

4.6.2.1 Drag from a random distribution of particles

For a volume fraction F_V of randomly distributed spherical particles of radius **r**, the number of particles per unit volume (N_V) is given (appendix 2.8) by

$$N_V = \frac{3\,F_V}{4\pi\,r^3} \tag{4.21}$$

If the boundary is planar, then particles within a distance **r** on either side of the boundary will intersect it. Therefore the number of particles intersecting unit area of the boundary is

$$N_S = 2rN_V = \frac{3F_V}{2\pi\,r^2} \tag{4.22}$$

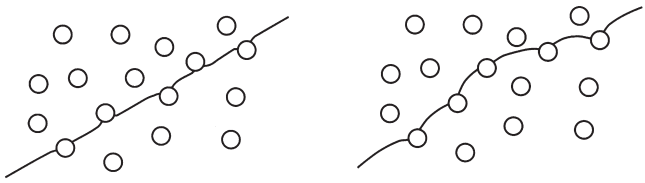

(a) (b)

Fig. 4.24. Interaction of particles with (a) a rigid planar boundary; (b) a flexible boundary.

The pinning pressure exerted by the particles on unit area of the boundary is given by

$$P_Z = N_S F_S \tag{4.23}$$

and hence from equations 4.12 and 4.22

$$P_Z = \frac{3F_V\gamma}{2r} \tag{4.24}$$

This type of relationship was first proposed by Zener (Smith 1948), although in the original paper because N_S was taken as r. N_V, the pinning pressure was half that of equation 4.21. P_Z as given by equation 4.24 is commonly known as the **Zener pinning pressure.**

It is clear that this calculation is not rigorous, because if the boundary is rigid as is assumed, then as many particles will be pushing the boundary one way as will be pulling it the other as shown in figure 4.24a, and the net pinning pressure will be nil. (This is a similar problem to that encountered in calculating the interaction of a dislocation with an array of solute atoms). Therefore the boundary must relax locally from a planar configuration, as shown in figure 4.24b, if pinning is to occur.

More rigorous calculations of the Zener drag have been attempted by many authors, and the reader is referred to the reviews by Nes et al. (1985), Hillert (1988) and Doherty et al. (1989) for further details. However, it is concluded that the more sophisticated calculations do not lead to relationships which differ significantly from equation 4.24, which remains widely used. Although some early computer simulations suggested that the Zener drag was not given correctly by equation 4.24, more recent simulations by Miodownic et al. (2000) have confirmed the Zener relationship (see also §11.4.2).

4.6.2.2 Effects of boundary-particle correlation

The assumption of a planar or near planar boundary as required to give the Zener pinning pressure of equation 4.24 will only be reasonable if the grain or subgrain size is very much larger than the interparticle spacing, as pointed out by Anand and Gurland (1975), Hellman and Hillert (1975), Hutchinson and Duggan (1978), Hillert (1988), and Hunderi and Ryum (1992a). If this is not the case, then we need to examine, albeit in a

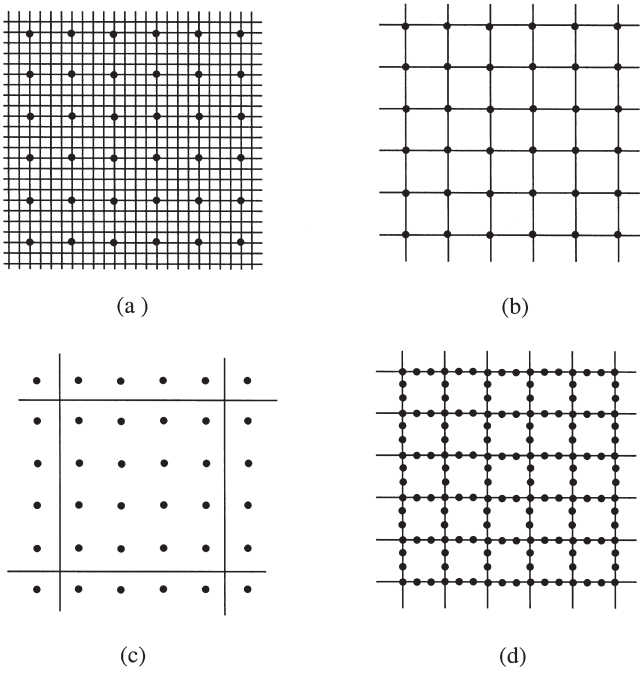

Fig. 4.25. Schematic diagram of the correlation between particles and boundaries as a function of grain size.

simplified way, the consequences. In figure 4.25 we identify four important cases. In figure 4.25a the grains are much smaller than the particle spacing, in figure 4.25b the particle spacing and grain size are similar, in figure 4.25c the grain size is much larger than the particle spacing and in figure 4.25d, the particles are inhomogeneously distributed so as to lie only on the boundaries. In all these cases there is a strong correlation between the particles and the boundaries, although an accurate assessment of the pinning force is difficult and is dependent on the details of the particle and grain (or subgrain) arrangement.

Consider the particles and boundaries which form the three-dimensional cubic arrays shown in figure 4.25. For case **a**, it is reasonable to assume that all the particles lie not only on boundaries, but at vertices in the grain structure, because in these positions the particles, by removing the maximum boundary area, minimise the energy of the system.

If the grain edge length is **D**, then the grain boundary area per unit volume is 3/D. The number of particles per unit area of boundary (N_A) is given by

$$N_A = \frac{\delta N_V D}{3} \tag{4.25}$$

where δ is a factor which depends on the positions of the particles in the boundaries. For particles on boundary faces, $\delta = 1$. For particles at the vertices as shown in figures 4.25

(a) and (b), $\delta = 3$ and hence, using equation 4.21

$$N_A = \frac{\delta N_V D}{3} = \frac{3DF_V}{4\pi r^3} \tag{4.26}$$

For incoherent spherical particles the pinning pressure on the boundary (P'_Z) will then be given by

$$P'_Z = F_S N_A = \frac{3DF_V\gamma}{4r^2} \tag{4.27}$$

This relationship will be valid for grain sizes up to and including that shown in figure 4.25b, in which the grain size and particle spacing are the same (D_C). In this situation, the spacing of the particles on the cubic lattice (L) is equal to D_C and is given by

$$L = D_C = N_V^{-1/3} = \left(\frac{4\pi r^3}{3F_V}\right)^{1/3} \tag{4.28}$$

at which point the pinning force reaches a maximum $P'_{Z\max}$ given by

$$P'_{Z\max} \approx \frac{1.2\gamma F_V^{2/3}}{r} \tag{4.29}$$

As the grain size increases beyond D_C, the number of particles per unit area of boundary (N_A) will decrease from that given by equation 4.26 and eventually reach N_S as given by equation 4.22. We can treat this transition from correlated to non-correlated boundary in the following approximate manner.

The number of boundary corners per unit volume in a material of grain size **D** is given approximately by $1/D^3$, and the fraction of particles lying on these potent pinning sites is therefore, for the condition $D \geq D_C$.

$$X = \frac{1}{N_V D^3} \tag{4.30}$$

When $D = D_C$ then from equation 4.28 we find $X = 1$. Thus as the grains grow, a diminishing fraction of particles is able to sit at the grain corners.

The number of corner-sited particles per unit area of boundary is then

$$N_C = XN_V D \tag{4.31}$$

The remaining particles will sit on grain boundaries or grain edges or lie within the grains. In this simple analysis we assume that the particles which are not sitting at grain corners are intersected at random by boundaries and therefore the number per unit area is

$$N_r = 2rN_V(1 - X) \tag{4.32}$$

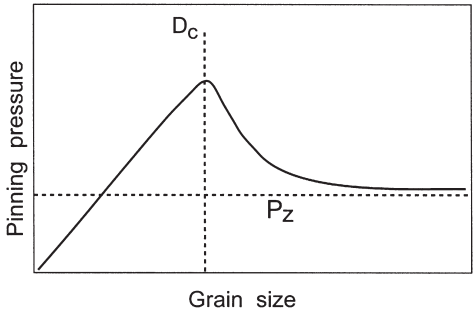

Fig. 4.26. The effect of grain size on the Zener pinning force for a given particle dispersion.

Thus the total number of particles per unit area of boundary is $N_c + N_r$ and, using equation 4.23, the pinning pressure is given by

$$P''_Z = \pi r \gamma [X\, N_V\, D + (1 - X) 2\, N_V\, r] \tag{4.33}$$

or, when $D \geq D_C$

$$P''_Z = \pi r \gamma \left(\frac{1}{D_2} + (1 - \frac{1}{N_V\, D^3}) 2\, N_V\, r \right) \tag{4.34}$$

In figure 4.26, we show the pinning pressure on the boundary as a function of the grain size. It can be seen that as the grain size increases, the pinning pressure rises according to equation 4.27, peaks when the grain size approaches D_C and eventually falls (equation 4.33) to the Zener pinning pressure as given by equation 4.24.

It should be noted that actual values of the peak pinning pressure discussed here are based on a very simple geometry and are not accurate. However, the principle that the pinning pressure varies in a manner similar to that shown in figure 4.26 is undoubtedly correct and has some important implications for recovery, recrystallization and grain growth of particle-containing materials which will be discussed in later chapters.

4.6.2.3 Drag from non-random particle distributions

In many alloys the particles may not be randomly distributed. Of particular importance is the situation in which the particles are concentrated in planar bands as shown in figure 4.27. This type of structure is often found in rolled products such as Al-killed steels, most commercial aluminium alloys, and products made by powder metallurgy. In many cases the individual particles are also rod or plate-like and aligned parallel to the rolling plane. Nes et al. (1985) have modelled the case shown in figure 4.27a and have calculated the grain aspect ratio following primary recrystallization.

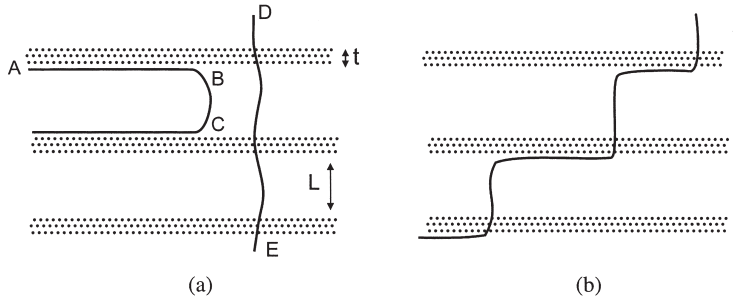

Fig. 4.27. The interaction of boundaries with planar arrays of particles. (a) The effect of boundary orientation on pinning; (b) Propagation of a boundary through planar arrays of particles, (after Nes et al. 1985).

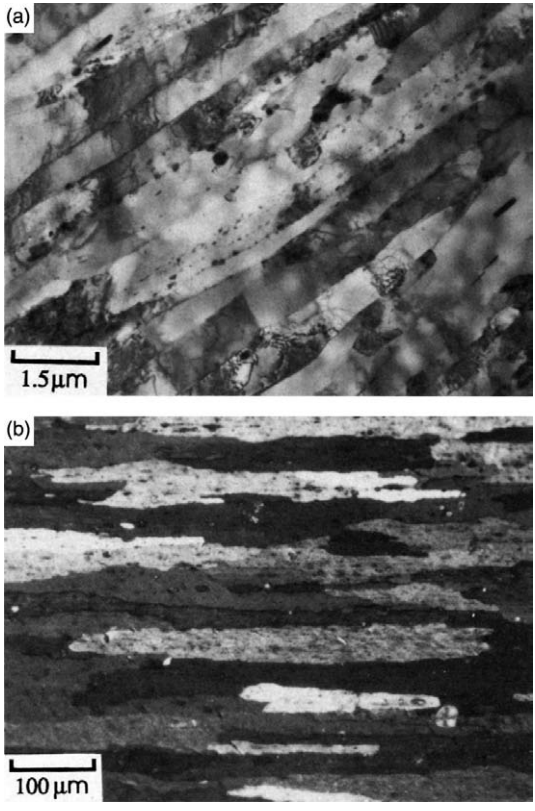

Fig. 4.28. (a) Transmission electron micrograph illustrating the pinning of low angle boundaries by planar arrays of small oxide particles in a rolled aluminium billet produced by powder metallurgy, (TD plane sections); (b) Optical micrograph of the same material after recrystallization showing an elongated grain structure, (Bowen et al. 1993).

Let us assume that spherical particles of radius **r** are aggregated in bands of thickness **t**, which are spaced a distance of **L** apart. A boundary AB lying parallel to the planar bands experiences a drag

$$P_{PZ} = \frac{P_Z L}{t} \tag{4.35}$$

where P_Z is the drag pressure if the particles are uniformly distributed as given by equation 4.23.

The drag on a boundary lying perpendicular to the bands depends strongly on the shape of the boundary. For example the curved boundary segment BC in figure 4.27a does not experience any pinning. However, if the boundary is long, e.g. segment DE, and if the driving pressure is uniformly distributed the average pinning pressure is P_Z. In either case, the pinning force is significantly greater in the direction normal to the bands and this anisotropy will be reflected in the shape of the grains or subgrains. Nes et al. (1985) have shown that the boundary is expected to propagate in a staggered manner as shown in figure 4.27b. Figure 4.28a is a transmission micrograph of a rolled powder metallurgy aluminium sheet product showing how bands of small oxide particles interact with the **low angle boundaries** and affect the shape of the subgrains during recovery, and figure 4.28b is an optical micrograph of the same material after recrystallization, which clearly shows how interaction of the aligned oxide particles with **high angle boundaries** results in an elongated grain structure after recrystallization.

Another important situation in which non-random particle distribution may occur is when the second-phase particles are precipitated onto pre-existing low or high angle boundaries (e.g. Hutchinson and Duggan 1978). In this case, as shown schematically in figure 4.25d, all (or most) of the particles lie on the boundaries. The effective number of particles per unit area of boundary is given approximately by equation 4.27 with δ in equation 4.26 equal to 1, and the pinning force (P_X) by

$$P_X = F_S N_A = \frac{\gamma D F_V}{4r^2} \tag{4.36}$$